Lithium Thiophosphate Functionalized Zirconium MOFs for Li−S Batteries with Enhanced Rate Capabilities

Avery E. Baumann,[†] Xu Han,[†] Megan M. Butala,[‡,§] and V. Sara Thoi*,[†]

[†]Department of Chemistry, Johns Hopkins University, Baltimore, Maryland 21218, United States
[‡]Department of Materials Science and Engineering, University of Florida, Gainesville, Florida 32611-6400, United States
[§]Materials Measurement Science Division, National Institute of Standards and Technology, Gaithersburg, Maryland 20899, United States

S *Supporting Information*

ABSTRACT: Zirconium metal−organic frameworks (Zr-MOFs) are renowned for their extraordinary stability and versatile chemical tunability. Several Zr-MOFs demonstrate a tolerance for missing linker defects, which create "open sites" that can be used to bind guest molecules on the node cluster. Herein, we strategically utilize these sites to stabilize reactive lithium thiophosphate (Li_3PS_4) within the porous framework for targeted application in lithium−sulfur (Li−S) batteries. Successful functionalization of the Zr-MOF with PS_4^{3-} is confirmed by an array of techniques including NMR, XPS, and Raman spectroscopy, X-ray pair distribution function analysis, and various elemental analyses. During electrochemical cycling, we find that even a low incorporation extent of lithium thiophosphate in Zr-MOFs improves sulfur utilization and polysulfide encapsulation to deliver a sustainably high capacity over prolonged cycling. The functionalized MOF additives also prevent cell damage under abusive cycling conditions and recover high capacities when the cell is returned to lower charge/discharge rates, imperative for future energy storage devices. Our unique approach marries the promising chemical attributes of the purely inorganic Li_3PS_4 with the stability and high surface area of MOFs, creating a Li−S cathode architecture with a performance beyond the sum of its component parts. More broadly, this novel functionalization strategy opens new avenues for facile syntheses of "designer materials" where chemical components from discrete disciplines can be united and tailored for specific applications.
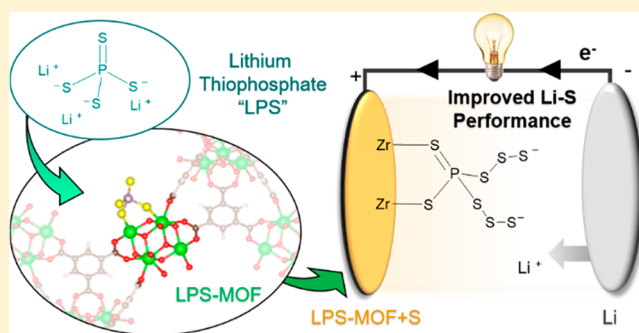
INTRODUCTION

Owing to their high stability, synthetic versatility, and porosity, zirconium metal−organic frameworks (Zr-MOFs) have been widely used in chemical storage and separations, catalysis, chemical sensing, and drug delivery.[1−4] Zr-MOFs with a hexanuclear zirconium node structure are amenable to missing linker or cluster defects and postsynthetic modification, affording high chemical and physical tunability.[5−9] These defects produce "open sites" on the Zr centers where the multitopic organic linker is not present. The open sites are available to bind substrates for chemical transformation, while the acidic protons in the defected cluster can facilitate catalytic hydrolysis reactions.[3,4,10] For instance, Zr-MOFs catalyze organophosphate hydrolysis and have been used to neutralize chemical warfare agents.[11−16] Functionalized NU-1000 and MOF-808 utilize these open sites to anchor phosphate (PO_4^{3-}) or sulfate (SO_4^{2-}) groups to enable efficient catalytic organic reactions.[10,17,18] Beyond chemical conversion, open sites on the Zr-MOF node have an affinity for contaminants such as arsenic,[19] antimony,[20] lead,[21,22] and various other metal ions[23,24] with a demonstrated efficacy in water purification.

Inspired by the versatile functionality of Zr nodes with phosphates and other small ionic molecules, we synthesized a series of Zr-MOFs with a lithium thiophosphate moiety coordinated to the open sites to anchor soluble sulfur species in lithium−sulfur (Li−S) batteries (Scheme 1). The ability to sequester these polysulfide species diminishes the extent of active material leached from the cathode and prevents passivation of the anode surface by migrating sulfur species. Limiting both of these phenomena results in high capacity delivery and prolonged device lifetime, ultimately improving device performance.

Lithium phosphorus sulfide compounds, such as Li_3PS_4, $Li_7P_3S_{11}$, and $Li_2S−P_2S_5$ glasses, are well-known Li ion conductors that have been extensively studied as solid-state electrolytes in batteries.[25,26] However, their use as electrode additives in battery systems has been less explored.[27] In Li−S batteries, the thiophosphate moiety offers a solution to chemically tether soluble polysulfides and mitigate deposition of Li_2S/Li_2S_2 in the cathode architecture.[28,29] Phosphorus

Scheme 1. Demonstration of the Versatile Functionality of Zr-MOF Nodes in a Variety of Fields, from Chemical Transformation to Ion Sequestration[a]
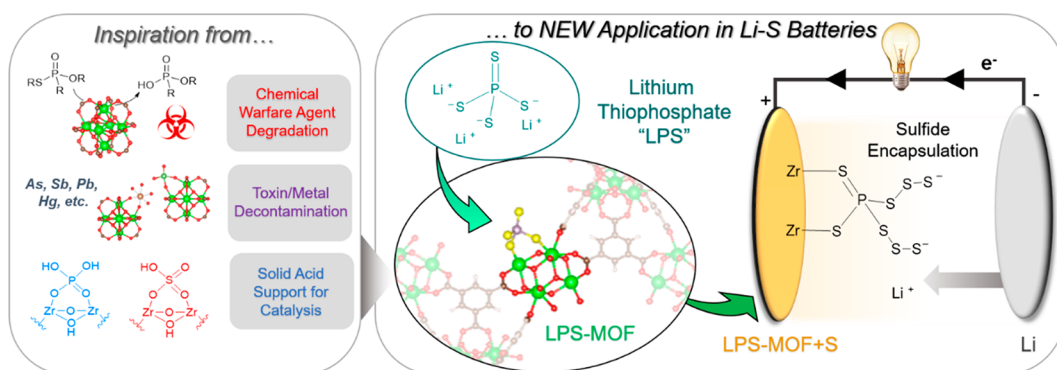
[a]Inspiration drawn from these applications culminate in our tethering design, in which anchoring the thiophosphate allows for stable, reversible cycling via the encapsulation of polysulfides within Li−S battery cathodes.

Scheme 2. Engineering of the Hexanuclear Node in Zr-MOFs To Contain Open Sites Capable of Binding Lithium Thiophosphate Guests[a]
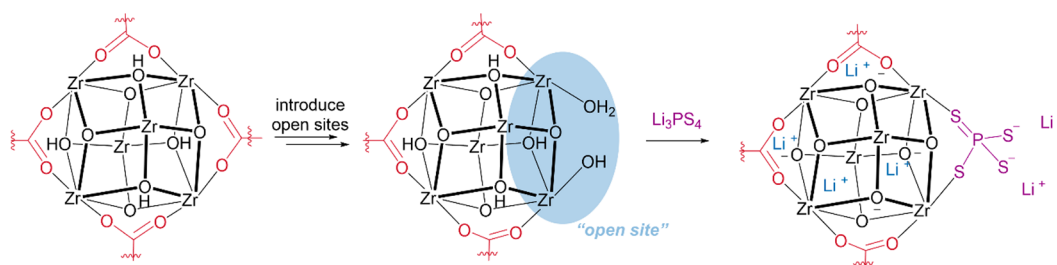
[a]Only one-third of the ligands are shown for clarity.

pentasulfide (P_2S_5) employed as an electrolyte additive exhibits demonstrated reactivity with lithium polysulfides to form $Li_{3+y}PS_{4+x}$ in solution via S−S bond formation.[29] However, the $Li_{3+y}PS_{4+x}$ molecules are also soluble in the electrolyte and can result in loss of active material from the cathode, limiting the cell capacity. We propose anchoring the PS_4^{3-} moiety will prevent its dissolution while also allowing S−S bond formation with sulfide species, effectively suppressing the leaching effect and improving battery performance.

Motivated by the extensive efforts to functionalize inorganic- and carbon-based materials,[30−35] we sought to bind PS_4^{3-} to the open sites on the MOF node. The innate porosity of the MOF enables the diffusion of Li_2S_x within the material and provides space for encapsulation via S−S bond formation, while the metal node securely anchors the thiophosphate within the cathode. In this study, we demonstrate the ability to quantitatively control thiophosphate loading into two zirconium MOFs, UiO-66 and MOF-808. A detailed chemical and structural investigation using spectroscopic techniques and pair distribution function analysis confirms binding of PS_4^{3-} at the metal node. The synthesized "LPS-MOFs" are applied as cathode additives in Li−S batteries, resulting in improved sulfur utilization and capacity retention under a variety of cycling conditions. Electrochemical characterization and postcycling analyses reveal that the thiophosphate moiety diminishes polysulfide leaching, resulting in a marked improvement in cycling performance in comparison to cells containing nonfunctionalized MOFs and those without any MOF additives. Furthermore, our functionalization strategy can be applied generally to the design of a variety of materials (MOFs, polymers, polyoxometalates, functionalized carbon, etc.) and illuminates a new avenue for the exploration of hybrid materials, exploiting the benefits of traditional solid-state materials in more accessible material platforms.

RESULTS AND DISCUSSION

Synthesis and Characterization. The node structure of Zr-MOFs features six metal atoms connected by bridging hydroxo, oxo, and carboxylate ligands. In a fully coordinated node, 12 carboxylates bridge each Zr atom to its neighboring atom and prevent interaction with guest species. If a portion of the nodal carboxylate ligands is removed, "open sites" (highlighted in Scheme 2) become available to bind guest molecules, providing synthetic handles for the advanced functionalization of the metal node. Several Zr-MOFs are capable of supporting these open sites, either through the inherent crystal structure (MOF-808) or by introduction of defects using a modulated synthetic approach (UiO-66).[6,7] Herein, we employ these open sites to chemically tether PS_4^{3-} within the MOF structure. A series of MOFs, **UiO-66(noMod)**, **UiO-66(50Benz)**, and **MOF-808**, was synthesized by modifying previously reported procedures.[6,7,36] Potentiometric acid−base titration of each MOF (Figure S1) and BET surface area analysis were used to gauge the number of open sites (Table S1).[6,7,36−38] The varying number of open sites per node in **UiO-66(noMod)**, **UiO-66(50Benz)**, and **MOF-808** provide a platform to systematically regulate the incorporation of guest molecules at the Zr node.

We next developed a method to incorporate the PS_4^{3-} moiety at these open sites while preserving the structure of the

MOF. Our efforts were complicated by the tendency of Li_3PS_4 to undergo P−S bond hydrolysis in the presence of a proton source (as shown in an NMR experiment, Figure S2a) to release hydrogen sulfide (H_2S). In addition, both the MOFs and lithium thiophosphate are sensitive to solution conditions; Zr-MOFs are unstable in water at high pH, and Li_3PS_4 is insoluble in most solvents.[39] We discovered that Li_3PS_4 (synthesized following a previous report; see the Supporting Information for details) is relatively stable in a basic triethylamine (20% by volume) and methanol solution, herein referred to as "TEA-MeOH". To examine the reactivity of Li_3PS_4 with TEA and MeOH, we employed phosphorus nuclear magnetic resonance spectroscopy (^{31}P NMR). The ^{31}P NMR spectrum (Figure S2b) of the TEA-MeOH solution shows a predominant signal at 91 ppm (for the remainder of the solution NMR discussion, 1 ppm = 400 Hz), which is slightly shifted from the reported value of 87 ppm when Li_3PS_4 is dissolved under basic aqueous conditions. A low-intensity peak is observed at 128 ppm in TEA-MeOH solutions (Figure S2b). This phosphorus byproduct was not observed in the LPS-MOF samples (vide infra), suggestive that this species does not affect the loading of Li_3PS_4 into the MOF.

After evaluation of the reactivity of Li_3PS_4, successful loading of the thiophosphate was accomplished by soaking activated MOF powder in the TEA-MeOH loading solution containing ∼0.05 M Li_3PS_4. After extensive washing to remove unincorporated species, the lithium thiophosphate functionalized MOFs (LPS-MOFs) were analyzed by powder X-ray diffraction (XRD) and infrared spectroscopy (FT-IR) (Figure 1a and Figures S3 and S4), where the crystallinity and characteristic vibrational features are retained after the loading

procedure. Synthesized LPS-MOFs also show an increased tolerance to air exposure in comparison to the Li_3PS_4 solid as observed by FT-IR (Figure S5).

Elemental analyses confirmed that the extent of lithium thiophosphate loading is correlated with the number of open sites. The digested samples show increasing Li and P content in the order **UiO-66(noMod)** < **UiO-66(50Benz)** < **MOF-808** (Figure 1b and Table S2). Owing to its larger pore size and higher number of open sites, MOF-808 can incorporate additional PS_4^{3-} units when the stoichiometric loading ratio is increased from 0.7 to 2 equiv. Corroborating this result, the S:Zr elemental ratio from energy dispersive spectroscopy (EDS) also demonstrated that the number of open sites and stoichiometry used determine the quantity of incorporated thiophosphate (Table S2). However, our incorporation method only functionalized a fraction of the total available sites (Table S3), suggesting future method development may enable even greater thiophosphate integration.

The successful incorporation of the thiophosphate moiety was further confirmed by solution-state ^{31}P NMR spectroscopy. Functionalized LPS-MOFs were first soaked in an aqueous 1 M sodium hydroxide solution overnight to digest the MOF and release incorporated guest molecules. The ^{31}P NMR spectrum of digested **LPS-UiO-66(50Benz)** shows a single peak at 89 ppm (Figure 1c), which is assigned as PS_4^{3-}. For reference, partially hydrolyzed thiophosphate species, such as PS_3O^{3-}, $PS_2O_2^{3-}$, and PSO_3^{3-}, appear at shifts <86 ppm (Figure S2a), evincing that our synthetic conditions do not lead to P−S bond hydrolysis in the UiO-66 or MOF-808 samples (Figure S6).[40] Our characterization efforts thus prove that careful selection of both the solvent and base employed in the synthesis allows for the controllable loading of thiophosphate and preservation of the MOF structure.

To interrogate the nature of the thiophosphate in the framework, LPS-MOF samples were examined by solid-state ^{31}P NMR spectroscopy. The air-free solid-state ^{31}P NMR spectrum of **LPS-UiO-66(50Benz)** (Figure 1d) shows the existence of a phosphorus signal centered at 96.5 ppm (for the remainder of the solid-state NMR discussion, 1 ppm = 500 Hz), which confirms that the PS_4^{3-} moiety is not hydrolyzed during the loading procedure. This value is shifted from the solid-state Li_3PS_4 signal reported at 87 ppm, suggesting that the local environment of the encapsulated thiophosphate is chemically different from crystalline Li_3PS_4.[41] Additive scans taken over 24 h begin to show the development of a broad peak centered at 52 ppm, corresponding to a mixed P−S/P−O species formed via P−S bond hydrolysis due to air exposure in the sample holder (Figure S7). The phosphorus signal at −1 ppm is assigned to fully hydrolyzed phosphate and appears only after the first 6 h of exposure. A proposed degradation mechanism illustrating this process is provided in Scheme S1.

X-ray photoelectron spectroscopy (XPS) provides insight regarding the chemical environment of both the thiophosphate and Zr node in LPS-MOFs. Collected spectra demonstrate that both the Zr 3d and S 2p orbitals are electronically perturbed upon incorporation of PS_4^{3-} into the MOF structure (Figure 2 and Figure S8). The red shift in the binding energy of the Zr $3d_{5/2}$ orbital from 182.8 to 182.3 eV observed for the **2xLPS-MOF-808** sample suggests that the Zr node is binding to the thiophosphate moiety, which is less electronegative than the pair of aquo and hydroxide ligands. The spectrum also features a shoulder that can be fitted to values more appropriate for a Zr−S bonding environment than for Zr−O (Figure 2a).[42]
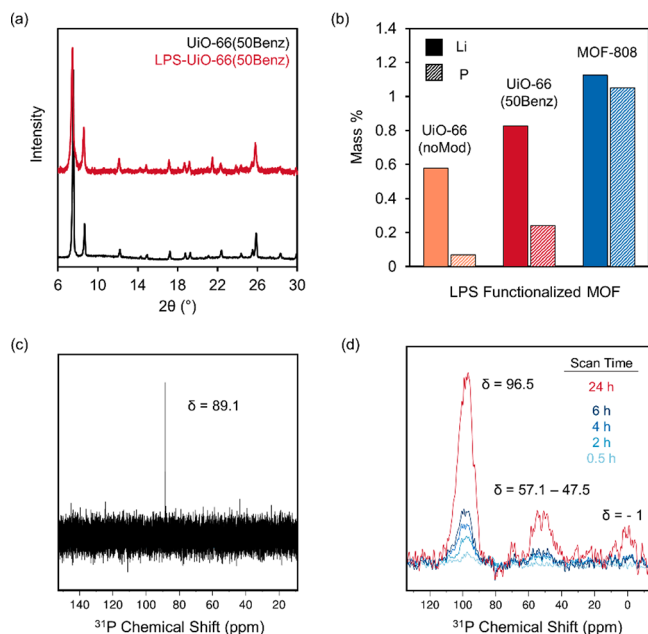

Figure 1. (a) XRD of **LPS-UiO-66(50Benz)** showing that MOF peaks remain intact after thiophosphate incorporation. (b) Tunable lithium thiophosphate loading attainable in LPS-MOF samples, evidenced by elemental quantification of Li (solid) and P (striped). ^{31}P NMR of (c) digested **LPS-UiO-66(50Benz)** in 1 M aqueous sodium hydroxide solution and (d) as-synthesized solid-state **LPS-UiO-66(50Benz)**, indicating that the thiophosphate remains intact. After extended air exposure, hydrolysis products are observable in the solid-state ^{31}P NMR (signal additive over time).
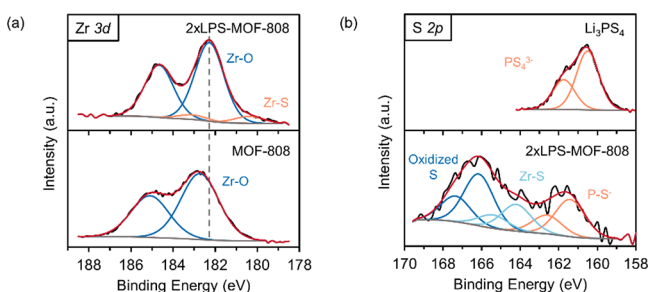
Figure 2. XPS of the (a) Zr 3d region in **MOF-808** and in **2xLPS-MOF-808** samples and (b) S 2p region in **2xLPS-MOF-808** and Li_3PS_4 samples, showing clear differences in binding energies when the thiophosphate species is incorporated into the MOF.

Upon extended air exposure, the peak at 182.3 eV is shifted positively to 182.5 eV, consistent with the replacement of some Zr−S bonds with Zr−O bonds via thiophosphate hydrolysis. We note that the changes in the Zr 3d spectrum are slight, as only a small fraction of Zr atoms are influenced by thiophosphate binding; the majority of the Zr centers are still bound to O ligands even after functionalization. More drastic changes are observed for the S 2p binding energy upon incorporation into the framework. The single S environment in Li_3PS_4 (S $2p_{3/2}$ binding energy of 160.5 eV) transforms to multiple distinct species observed in the **2xLPS-MOF-808** sample with binding energies of 166.2, 164.3, and 161.5 eV for the S $2p_{3/2}$ orbitals (Figure 2b). The 164.3 eV binding energy signal is consistent with sulfides bound to highly oxidized Zr^{4+} metal nodes, while the 161.5 eV signal is attributed to the unbound sulfur atoms on the same PS_4^{3-} group.[43−45] The binding energy of 166.2 eV is representative of oxidized sulfur species, which we attribute to the oxidation of the material surface during handling, as no S−O features are observed in the bulk material by Raman spectroscopy (Figure S9). XPS spectra of the P 2p region also corroborates that LPS-MOFs feature a thiophosphate environment different from that of Li_3PS_4, although the signal to noise is too low for a more substantive discussion (Figure S8). Perturbation of Zr, S, and P binding energies and the appearance of new sulfur and phosphorus environments are in line with our hypothesis that the thiophosphate moiety binds to the Zr node.

Raman spectroscopy provides another handle to probe the chemical changes in the functionalized Zr-MOFs (Figure 3a).

The low-frequency region from 200 to 400 cm^{-1} is important for characterizing the Zr node structure.[46] In the Raman spectra of **UiO-66(50Benz)**, two features at 250 and 280 cm^{-1} are attributed to Zr−O stretches, consistent with previous reports.[46,47] Upon introduction of thiophosphate, a broad feature dominates this region (the maximum intensity is at 273 cm^{-1}), indicating that the introduction of the thiophosphate alters the vibrational modes of the Zr node. This hypothesis is supported by the appearance of a broad feature centered at 323 cm^{-1}, consistent with previously assigned Zr−S stretching frequencies (Figure S9).[48,49] A new peak at 412 cm^{-1} is also present, again shifted slightly from the P−S stretching frequency in Li_3PS_4 (420 cm^{-1}).[41,50] After air exposure to the LPS-MOF, slight differences in the peak shape and position are observed in the Zr−O and Zr−S regions (Figure S9a), suggesting at least a portion of the thiophosphate molecules are removed from the node upon exposure to air. In combination with other characterization methods (vide infra), the apparent Raman shifts of the Zr node strongly support that PS_4^{3-} binds to the open sites on the Zr node.

Thermogravimetric analysis (TGA) also supports our hypothesis that PS_4^{3-} chemically reacts with the Zr node (Figure S10). In the derivative TGA, the decomposition of **LPS-UiO-66(50Benz)** is shifted to a higher temperature (550 °C) in comparison to that of the parent structure **UiO-66(50Benz)** (515 °C). Similarly, **MOF-808** also exhibits improved framework stability upon thiophosphate loading, as the decomposition temperature increases from 560 to 590 °C for **1xLPS-MOF-808**. Furthermore, TGA of the **1xLPS-MOF-808** sample exposed to air shows both MOF decomposition events at 560 and 590 °C, indicating that multiple node structures are present after partial thiophosphate hydrolysis.

X-ray pair distribution function (PDF) analysis elucidates additional structural information regarding the Zr node. X-ray PDF data for **MOF-808**, **1xLPS-MOF-808**, and **1xLPS-MOF-808** exposed to air show subtle differences in the positions and intensities of atom−atom correlations (Figure 3b and Figure S11). On comparison of first the **MOF-808** and **1xLPS-MOF-808** PDF data, shifts in the most prominent correlations, for Zr−O (~2.2 Å) and Zr−Zr (~3.5 Å), verify that the introduction of PS_4^{3-} influences the MOF node structure, consistent with our XPS, Raman, and TGA results. These values return to match those of the unloaded **MOF-808** sample upon air exposure, another common theme across our
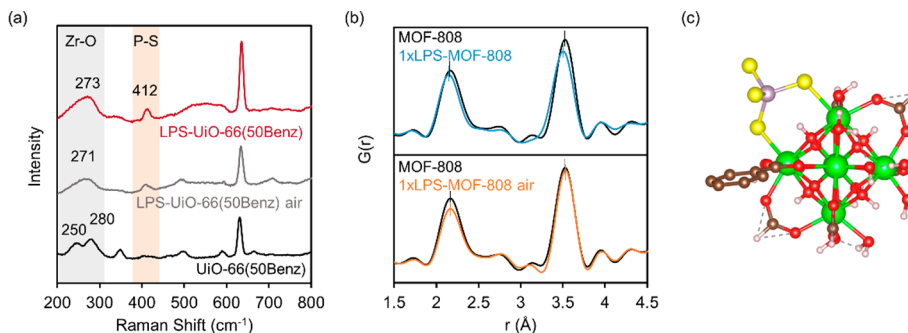

Figure 3. (a) Raman spectra of **UiO-66(50Benz)** and **LPS-UiO-66(50Benz)** collected under Ar and after exposure to air. Differences in the Zr−O and Zr−S regions upon introduction of PS_4^{3-} indicate binding at the Zr node. The peak at 412 cm^{-1} is attributed to the P−S bond. More detailed peak identifications are provided in the Supporting Information. (b) X-ray PDF data for **1xLPS-MOF-808** and **MOF-808** similarly indicating changes to the nodal structure, particularly in the Zr−O (~2.2 Å) and Zr−Zr (~3.5 Å) correlations. (c) Optimized thiophosphate bound node structure with one added linker, where Zr, S, P, O, C, and H atoms are shown in green, yellow, purple, red, brown, and white, respectively. Li atoms have been removed for clarity.

various characterization methods (a more detailed explanation is provided in Scheme S1). These results are consistent with simulated PDF of a single modified Zr node with one coordinated linker and one PS_4^{3-} molecule (Figure 3c, Figures S11−S14, and Table S4). Further discussions, peak identifications, simulated PDF patterns, and analyses are included in the Supporting Information. Our combined efforts detail that the chemical and structural changes imparted upon introducing PS_4^{3-} into the MOF confirm binding at the Zr node.

Electrochemistry and Li−S Cycling. With confidence that the PS_4^{3-} moiety is anchored within the MOF, we explored the electrochemical influence of LPS-MOFs in Li−S batteries. A homogenized slurry of 30% MOF (by mass), 45% sulfur, 15% Super-P carbon, and 10% PVDF was cast onto carbon paper disks in an Ar-filled glovebox to form the MOF composite cathodes. Once dry, the composite cathode and Li metal anode were assembled into a coin cell with a Celgard separator and an electrolyte of 1 M LiTFSI in equal volumes of DOL and DME with a 2% LiNO$_3$ additive (by mass). Cyclic voltammetry (CV) experiments on the coin cells (Figure S15) showed two cathodic events corresponding to the reduction of S$_8$ to Li$_2$S$_x$ ($x = 4−8$) and the reduction of long-chain polysulfides to short-chain polysulfides ($x < 4$). To observe the interactions between thiophosphate and sulfur in the MOF, **1x-LPS-MOF-808** was impregnated with molten sulfur (**LPS-MOF-808@S**). CVs of cells prepared with the sulfur-loaded MOF exhibit lower overpotentials for both reductive and oxidative events in comparison to those containing MOFs physically mixed with sulfur (Figure S16). Although preloaded **LPS-MOF-808@S** generally showed poor sulfur utilization due to a low sulfur loading, changes observed in CVs demonstrate that the thiophosphate in the MOF directly interacts with polysulfides electrochemically and plays a role in galvanostatic cycling. Furthermore, UV−vis spectroscopy of polysulfide solutions in the presence of the MOFs showed that the frameworks are able to sequester solubilized polysulfides effectively (Figure S17), leading to a visible color change of the LPS-MOF powders (Figure S18).

Li−S batteries are evaluated by both their deliverable maximum capacity and their ability to retain capacity through extended cycling. For galvanostatic cycling experiments, at least three coin cells of the same material were cycled at a charge/discharge rate ("C rate", where 1C = fully charged or discharged in 1 h) of C/10 (168 mA g^{-1} S) for 20 cycles, followed by 80 cycles at a rate of C/5 (336 mA g^{-1}) unless otherwise noted. The cycling performance of Li−S cells with **LPS-UiO-66(noMod)**, **LPS-UiO-66(50Benz)**, and **UiO-66** are shown in Figure 4a. LPS-MOF composite cathodes yield significantly higher maximum capacities than the analogous MOF electrodes, averaging 1193, 1172, and 891 mAh g^{-1} for **LPS-UiO-66(50Benz)**, **LPS-UiO-66(noMod)**, and **UiO-66**, respectively (Figure 5a). The increase in the maximum capacity is consistent with the increased lithium content measured by atomic absorption spectroscopy (AAS) (Table S2). This corroborates the conclusion from our previous study that increasing the Li ion concentration in Zr-MOFs improves sulfur utilization.[51] In addition to improved utilization, cells constructed with **LPS-UiO-66(noMod)** and **LPS-UiO-66-(50Benz)** demonstrate greater capacity retention than **UiO-66(50Benz)**. We also compared the performance of cells containing LPS-MOF and Li-MOF (lithiated analogues) from our previous report (Figure S19 and Table S5). The added Li ions in the cathode (imparted by the deprotonation/lithiation
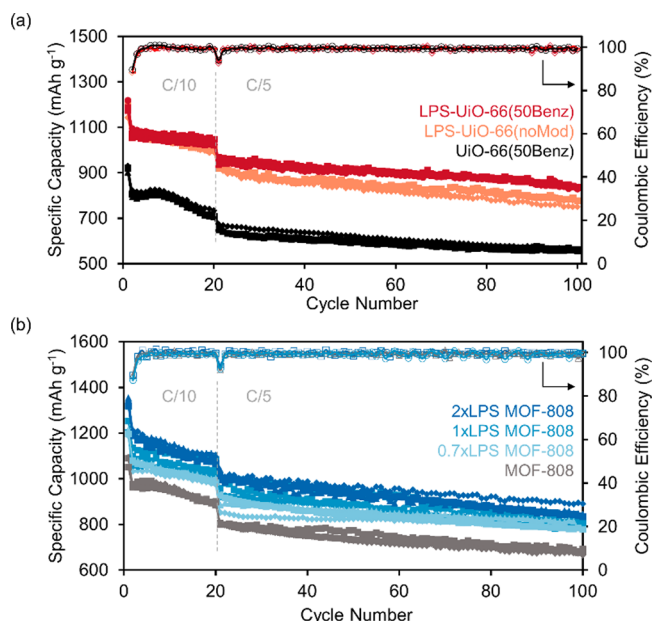

Figure 4. Cycling results for (a) UiO-66- and (b) MOF-808-containing cells, showing improvements in the maximum capacity and capacity retention upon lithium thiophosphate incorporation.
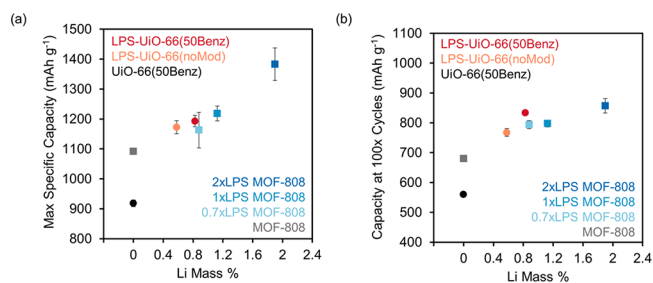

Figure 5. Compiled galvanostatic cycling results for (a) maximum capacity and (b) capacity after 100 cycles for various MOF composite cells. Both graphs generally show that increased lithium thiophosphate incorporation (represented by Li mass %) results in increased capacity delivery. Error bars represent the standard deviation of the measured values.

approach or via Li$_3$PS$_4$) increased maximum deliverable capacity in both cases in comparison to unfunctionalized **UiO-66(50Benz)**; however, capacity retention is significantly improved in the LPS-MOF cells in comparison to the Li-MOF cells. We attribute this capacity retention to improved polysulfide encapsulation afforded by the thiophosphate moiety. After 100 cycles (20× C/10, 80× C/5), the **LPS-UiO-66(50Benz)** and **LPS-UiO-66(noMod)** composite cathodes have average specific capacities of 835 and 767 mAh g^{-1}, in comparaison to only 560 mAh g^{-1} for the **UiO-66(50Benz)** composites (Figure 5b). Notably, the MOFs remains intact after cycling, as evidenced by TGA of the recoverd cathodes.

MOF-808 has more open sites than UiO-66, enhancing its ability to bind additional equivalents of the thiophosphate guest. From our LPS-UiO-66 results, we expect both the maximum capacity and the capacity retention to increase with increasing thiophosphate incorporation. Composite cathodes of LPS-MOF-808 samples synthesized using 0.7, 1, and 2 stoichiometric equiv were assembled into cells and cycled galvanostatically using the same procedure as for the LPS-UiO-66 series (Figure 4b). The compiled results in Figure 5a exhibit

a clear trend in maximum capacity delivery, with an average improvement over **MOF-808** cells of ~70, 130, and 300 mAh g^{-1} for **0.7x-**, **1x-**, and **2x-LPS-MOF-808** samples, respectively. Increased capacity is again attributed to the increased Li content within the functionalized MOF. After 100 cycles, the capacity retention resembles that of the LPS-UiO-66 series, with **0.7x-**, **1x-**, and **2x-LPS-MOF-808** cells delivering capacities of ~800 mAh g^{-1}, whereas the cells containing nonfunctionalized **MOF-808** average less than ~700 mAh g^{-1}(Figure 5b). These observations suggest that the development of a more efficient loading method to increase thiophosphate incorporation would result in further improvements to cycling performance. Additionally, all cells constructed with LPS-MOF additives exhibit higher capacity retention in comparison to sulfur−carbon composite cathodes (45% S/C) (Figures S20 and S21).

Control experiments using electrodes constructed with **2xLPS-MOF-808** with no added S were examined by both voltammetric (Figure S22) and galvanostatic (Figure S23) electrochemical tests. The results demonstrate that the LPS-MOF additive provides negligible electrochemical contribution by itself. To further probe the role of the MOF in cycling performance, a nonporous zirconium scaffold, ZrO_2, was also used as a control additive. Metal oxides have been previously explored as additives for Li−S batteries owing to their ability to chemisorb polysulfides.[52−57] The surface of ZrO_2 is decorated with dangling hydroxides that can bind phosphates, carboxylates, and other oxygen-rich molecules.[58−61] However, ZrO_2 lacks the internal porosity afforded by MOFs. When ZrO_2 is subjected to the same loading procedure as for the Zr-MOFs, the resulting sample (**LPS-ZrO$_2$**) has a relatively low Li content, as measured by Li AAS, but a high S:Zr ratio according to surface measurements by EDS (Table S2), suggesting that PS_4^{3-} incorporation into ZrO_2 is low and is concentrated on the surface of the particles. Coin cells containing ZrO_2 exhibit performance similar to that of the cells with nonfunctionalized MOFs, while the **LPS-ZrO$_2$** cells fail within the first 100 cycles (Figure S24). In contrast to LPS-MOFs, **LPS-ZrO$_2$** is unable to securely contain the thiophosphate within the cathode, resulting in dissolution and rapid cell failure.

Examination of coin cells by electrochemical impedance spectroscopy (EIS) after cycling reveals the nature of the capacity decay. LPS-MOF-containing cells exhibit a lower electrode surface resistance in comparison to nonfunctionalized MOF, S/C, and LPS-ZrO$_2$ composite cells (Figures S25−S27), signifying that both the thiophosphate moiety and MOF together mitigate electrode passivation by decreasing polysulfide leaching from the cathode. Examination of the electrodes after cycling further validates this observation (Figures S28−S30). On the Li anode, dark yellow deposits are especially prevalent in the **LPS-ZrO$_2$** cell. Elemental analysis of the dark substance by EDS reveals a high sulfur content, suggestive of a significant polysulfide dissolution from the cathode. An investigation of cells containing LPS-MOF composite cathodes showed a lesser degree of sulfur deposition on the anode, indicating that polysulfides are leached to a lesser extent in the presence of the functionalized MOFs.

Motivated by the improved capacity delivery and retention observed in LPS-MOF composite cells, we also explored their performance under more arduous cycling conditions. The **LPS-UiO-66(50Benz)** composite cell exhibits higher capacities in comparison to **UiO-66(50Benz)** at all C rates (Figure

6a,b), owing to enhanced sulfur utilization and polysulfide retention. Moreover, when it is returned to a lower C rate of
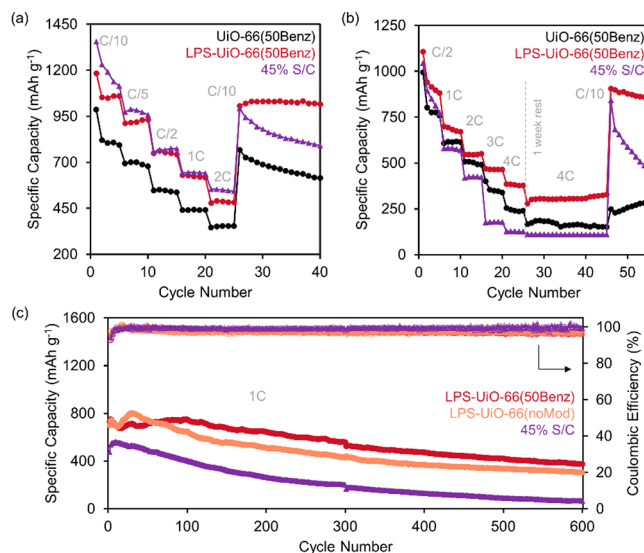

Figure 6. Rate capabilities for cells constructed using **LPS-UiO-66(50Benz)**, **UiO-66(50Benz)**, and 45% S/C cathodes at (a) low to moderate charge rates (C/10−2C), and (b) moderate to high charge rates (C/2−4C). **LPS-UiO-66(50Benz)**-containing cells deliver high capacities at a variety of C rates and are able to recover capacity when they are returned to C/10. (c) Extended galvanostatic cycling profiles at 1C further demonstrating that LPS-UiO-66-containing cathodes outperform S/C in initial capacity and capacity retention.

C/10, the **LPS-UiO-66(50Benz)** cell is remarkably able to recover and maintain a capacity of ~1040 mAh g^{-1}, identical with the capacity after its first five cycles at C/10. In contrast, **UiO-66(50Benz)** and 45% S/C cells are unable to fully recover and maintain this capacity, losing nearly 200 mAh g^{-1} in just 15 cycles. This superior ability of **LPS-UiO-66(50Benz)** to recover capacity is apparent even after the cells have been abused by continual cycling at charge rates up to 4C and prolonged storage in the discharged state. When the C rate is slowed to C/10 after these harsh cycling conditions, the **LPS-UiO-66(50Benz)** cell provides a capacity of 940 mAh g^{-1}, while the **UiO-66(50Benz)** cell can only reach 250 mAh g^{-1} and the 45% S/C cell irreversibly decays to zero capacity. The results of these experiments are distinct from those for the analogous lithiated samples analyzed in our previous report, where even a sample with higher Li mass % but lacking PS_4^{3-} cannot recover or retain capacity to the same extent (Figure S19 and Table S5).[51]

Cells constructed with LPS-MOF composite cathodes also show improved capacity delivery and retention in long-term cycling experiments at a C rate of 1C (Figure 6c). **LPS-UiO-66(50Benz)** and **LPS-UiO-66(noMod)** composite cathodes can deliver ~375 and ~300 mAh g^{-1} after 600 cycles, respectively, whereas the 45% S/C cell is unable to retain even 100 mAh g^{-1}. This improvement over S/C is unprecedented in MOF composite cathode reports.[62] Both variable C rate and long-term cycling experiments were also conducted using **2xLPS-MOF-808** composite cells, demonstrating results similar to those for the **UiO-66** system (Figure S31). Future studies will aim to increase thiophosphate incorporation within the MOF, utilizing alternative loading methods to further mitigate polysulfide leaching from the cathode.

CONCLUSION

In summary, we report the first account of utilizing lithium thiophosphates encapsulated in Zr MOFs for polysulfide capture. Our novel strategy takes advantage of the host–guest chemistry of the functionalized framework to stabilize these reactive species by slowing down P–S bond hydrolysis. Through extensive chemical and structural characterization, we establish PS_4^{3-} binds to the open sites of the Zr nodes in a fashion that parallels reports of phosphate- and sulfate-functionalized Zr-MOFs. Tethering the PS_4^{3-} group to the porous support of the MOF allows for reversible formation of S–S bonds with solubilized polysulfides formed during Li–S cycling, while thwarting the harmful dissolution of polysulfides and thiophosphate into the electrolyte. The benefits of thiophosphate incorporation are manifested in improved capacity delivery and retention at a variety of charge/discharge rates, where the overall performance gained is greater than the sum of the effects of the individual components. The rate capabilities and remarkable capacity recovery after abusive cycling are unparalleled in composite MOF Li–S cathodes. Our general strategy developed here motivates exploration of future discipline-transcending materials, where compound-specific shortcomings can be overcome using MOF hosts. Further studies are currently underway to examine the mechanisms of ion transport and electrochemical phenomena within these LPS-MOF devices.

ASSOCIATED CONTENT

Ⓢ Supporting Information

The Supporting Information is available free of charge on the ACS Publications website at DOI: 10.1021/jacs.9b09538.

> Methods, additional characterization data, and electrochemical experiment results (PDF)

AUTHOR INFORMATION

Corresponding Author

*E-mail for V.S.T.: sarathoi@jhu.edu.

ORCID Ⓞ

Avery E. Baumann: 0000-0001-8513-8049

V. Sara Thoi: 0000-0003-0896-4077

Notes

The authors declare no competing financial interest.

ACKNOWLEDGMENTS

REFERENCES

(1) Chen, Z.; Hanna, S. L.; Redfern, L. R.; Alezi, D.; Islamoglu, T.; Farha, O. K. Reticular Chemistry in the Rational Synthesis of Functional Zirconium Cluster-Based MOFs. *Coord. Chem. Rev.* **2019**, *386*, 32–49.

(2) Abánades Lázaro, I.; Forgan, R. S. Application of Zirconium MOFs in Drug Delivery and Biomedicine. *Coord. Chem. Rev.* **2019**, *380*, 230–259.

(3) Bai, Y.; Dou, Y.; Xie, L. H.; Rutledge, W.; Li, J. R.; Zhou, H. C. Zr-Based Metal-Organic Frameworks: Design, Synthesis, Structure, and Applications. *Chem. Soc. Rev.* **2016**, *45* (8), 2327–2367.

(4) Yuan, S.; Qin, J. S.; Lollar, C. T.; Zhou, H. C. Stable Metal-Organic Frameworks with Group 4 Metals: Current Status and Trends. *ACS Cent. Sci.* **2018**, *4* (4), 440–450.

(5) Cai, G.; Jiang, H. L. A Modulator-Induced Defect-Formation Strategy to Hierarchically Porous Metal-Organic Frameworks with High Stability. *Angew. Chem., Int. Ed.* **2017**, *56* (2), 563–567.

(6) Shearer, G. C.; Vitillo, J. G.; Atzori, C.; Bonino, F.; Bordiga, S.; Svelle, S.; Lillerud, K. P. Functionalizing the Defects: Post Synthetic Ligand Exchange in Metal Organic Framework UiO-66. *Chem. Mater.* **2016**, *28* (20), 7190–7193.

(7) Shearer, G. C.; Chavan, S.; Bordiga, S.; Svelle, S.; Olsbye, U.; Lillerud, K. P. Defect Engineering: Tuning the Porosity and Composition of the Metal-Organic Framework UiO-66 via Modulated Synthesis. *Chem. Mater.* **2016**, *28* (11), 3749–3761.

(8) Dissegna, S.; Epp, K.; Heinz, W. R.; Kieslich, G.; Fischer, R. A. Defective Metal-Organic Frameworks. *Adv. Mater.* **2018**, *30*, 1704501.

(9) Taddei, M. When Defects Turn into Virtues: The Curious Case of Zirconium-Based Metal-Organic Frameworks. *Coord. Chem. Rev.* **2017**, *343*, 1–24.

(10) Yabushita, M.; Li, P.; Islamoglu, T.; Kobayashi, H.; Fukuoka, A.; Farha, O. K.; Katz, A. Selective Metal-Organic Framework Catalysis of Glucose to 5-Hydroxymethylfurfural Using Phosphate-Modified NU-1000. *Ind. Eng. Chem. Res.* **2017**, *56* (25), 7141–7148.

(11) Bobbitt, N. S.; Mendonca, M. L.; Howarth, A. J.; Islamoglu, T.; Hupp, J. T.; Farha, O. K.; Snurr, R. Q. Metal-Organic Frameworks for the Removal of Toxic Industrial Chemicals and Chemical Warfare Agents. *Chem. Soc. Rev.* **2017**, *46* (11), 3357–3385.

(12) de Koning, M. C.; van Grol, M.; Breijaert, T. Degradation of Paraoxon and the Chemical Warfare Agents VX, Tabun, and Soman by the Metal-Organic Frameworks UiO-66-NH₂, MOF-808, NU-1000, and PCN-777. *Inorg. Chem.* **2017**, *56* (19), 11804–11809.

(13) Plonka, A. M.; Wang, Q.; Gordon, W. O.; Balboa, A.; Troya, D.; Guo, W.; Sharp, C. H.; Senanayake, S. D.; Morris, J. R.; Hill, C. L.; Frenkel, A. I. In Situ Probes of Capture and Decomposition of Chemical Warfare Agent Simulants by Zr-Based Metal Organic Frameworks. *J. Am. Chem. Soc.* **2017**, *139*, 599–602.

(14) Chen, H.; Liao, P.; Mendonca, M. L.; Snurr, R. Q. Insights into Catalytic Hydrolysis of Organophosphate Warfare Agents by Metal-Organic Framework NU-1000. *J. Phys. Chem. C* **2018**, *122*, 12362–12368.

(15) Wang, G.; Sharp, C.; Plonka, A. M.; Wang, Q.; Frenkel, A. I.; Guo, W.; Hill, C.; Smith, C.; Kollar, J.; Troya, D.; Morris, J. R. Mechanism and Kinetics for Reaction of the Chemical Warfare Agent Simulant, DMMP(*g*), with Zirconium(IV) MOFs: An Ultrahigh-Vacuum and DFT Study. *J. Phys. Chem. C* **2017**, *121* (21), 11261–11272.

(16) Troya, D. Reaction Mechanism of Nerve-Agent Decomposition with Zr-Based Metal Organic Frameworks. *J. Phys. Chem. C* **2016**, *120* (51), 29312–29323.

(17) Trickett, C. A.; Osborn Popp, T. M.; Su, J.; Yan, C.; Weisberg, J.; Huq, A.; Urban, P.; Jiang, J.; Kalmutzki, M. J.; Liu, Q.; Baek, J.; Head-Gordon, M. P.; Somorjai, G. A.; Reimer, J. A.; Yaghi, O. M. Identification of the Strong Brønsted Acid Site in a Metal-Organic Framework Solid Acid Catalyst. *Nat. Chem.* **2019**, *11*, 170.

(18) Jiang, J.; Gándara, F.; Zhang, Y. B.; Na, K.; Yaghi, O. M.; Klemperer, W. G. Superacidity in Sulfated Metal-Organic Framework-808. *J. Am. Chem. Soc.* **2014**, *136* (37), 12844−12847.

(19) Wang, C.; Liu, X.; Chen, J. P.; Li, K. Superior Removal of Arsenic from Water with Zirconium Metal-Organic Framework UiO-66. *Sci. Rep.* **2015**, *5*, 1−10.

(20) Li, J.; Li, X.; Hayat, T.; Alsaedi, A.; Chen, C. Screening of Zirconium-Based Metal-Organic Frameworks for Efficient Simultaneous Removal of Antimonite (Sb(III)) and Antimonate (Sb(V)) from Aqueous Solution. *ACS Sustainable Chem. Eng.* **2017**, *5* (12), 11496−11503.

(21) Yin, N.; Wang, K.; Wang, L.; Li, Z. Amino-Functionalized MOFs Combining Ceramic Membrane Ultrafiltration for Pb (II) Removal. *Chem. Eng. J.* **2016**, *306*, 619−628.

(22) Efome, J. E.; Rana, D.; Matsuura, T.; Lan, C. Q. Metal-Organic Frameworks Supported on Nanofibers to Remove Heavy Metals. *J. Mater. Chem. A* **2018**, *6* (10), 4550−4555.

(23) He, T.; Zhang, Y.; Kong, X.; Yu, J.; Lv, X.; Wu, Y.; Guo, Z.; Li, J. Zr(IV)-Based Metal-Organic Framework with T-Shaped Ligand: Unique Structure, High Stability, Selective Detection, and Rapid Adsorption of Cr 2 O 7 2- in Water. *ACS Appl. Mater. Interfaces* **2018**, *10* (19), 16650−16659.

(24) Liu, X.; Demir, N. K.; Wu, Z.; Li, K. Highly Water-Stable Zirconium Metal-Organic Framework UiO-66 Membranes Supported on Alumina Hollow Fibers for Desalination. *J. Am. Chem. Soc.* **2015**, *137* (22), 6999−7002.

(25) Chen, S.; Xie, D.; Liu, G.; Pierre, J.; Zhang, Q. Sul Fi de Solid Electrolytes for All-Solid-State Lithium Batteries: Structure, Conductivity, Stability and Application. *Energy Storage Mater.* **2018**, *14*, 58−74.

(26) Miura, A.; Rosero-Navarro, N. C.; Sakuda, A.; Tadanaga, K.; Phuc, N. H. H.; Matsuda, A.; Machida, N.; Hayashi, A.; Tatsumisago, M. Liquid-Phase Syntheses of Sulfide Electrolytes for All-Solid-State Lithium Battery. *Nat. Rev. Chem.* **2019**, *3* (3), 189−198.

(27) Lin, Z.; Liu, Z.; Dudney, N. J.; Liang, C. Lithium Superionic Sulfide Cathode for All-Solid Lithium-Sulfur Batteries. *ACS Nano* **2013**, *7* (3), 2829−2833.

(28) Lin, Z.; Liu, Z.; Fu, W.; Dudney, N. J.; Liang, C. Lithium Polysulfidophosphates: A Family of Lithium-Conducting Sulfur-Rich Compounds for Lithium-Sulfur Batteries. *Angew. Chem., Int. Ed.* **2013**, *52* (29), 7460−7463.

(29) Lin, Z.; Liu, Z.; Fu, W.; Dudney, N. J.; Liang, C. Phosphorous Pentasulfide as a Novel Additive for High-Performance Lithium-Sulfur Batteries. *Adv. Funct. Mater.* **2013**, *23* (8), 1064−1069.

(30) Liang, X.; Garsuch, A.; Nazar, L. F. Sulfur Cathodes Based on Conductive MXene Nanosheets for High-Performance Lithium-Sulfur Batteries. *Angew. Chem., Int. Ed.* **2015**, *54* (13), 3907−3911.

(31) Park, J.; Yu, B. C.; Park, J. S.; Choi, J. W.; Kim, C.; Sung, Y. E.; Goodenough, J. B. Tungsten Disulfide Catalysts Supported on a Carbon Cloth Interlayer for High Performance Li-S Battery. *Adv. Energy Mater.* **2017**, *7* (11), 1602567.

(32) Hart, C. J.; Cuisinier, M.; Liang, X.; Kundu, D.; Garsuch, A.; Nazar, L. F. Rational Design of Sulphur Host Materials for Li-S Batteries: Correlating Lithium Polysulphide Adsorptivity and Self-Discharge Capacity Loss. *Chem. Commun.* **2015**, *51* (12), 2308−2311.

(33) Doan-Nguyen, V. V. T; Subrahmanyam, K. S.; Butala, M. M.; Gerbec, J. A.; Islam, S. M.; Kanipe, K. N.; Wilson, C. E.; Balasubramanian, M.; Wiaderek, K. M.; Borkiewicz, O. J.; Chapman, K. A.; Chupas, P. J.; Moskovits, M.; Dunn, B. D.; Kanatzidis, M. G.; Seshadri, R. Molybdenum Polysulfide Chalcogels as High-Capacity, Anion-Redox-Driven Electrode Materials for Li-Ion Batteries. *Chem. Mater.* **2016**, *28* (22), 8357−8365.

(34) Zhou, G.; Paek, E.; Hwang, G. S.; Manthiram, A. Long-Life Li/Polysulphide Batteries with High Sulphur Loading Enabled by Lightweight Three-Dimensional Nitrogen/Sulphur-Codoped Graphene Sponge. *Nat. Commun.* **2015**, *6*, 1−11.

(35) Preefer, M. B.; Oschmann, B.; Hawker, C. J.; Seshadri, R.; Wudl, F. High Sulfur Content Material with Stable Cycling in Lithium-Sulfur Batteries. *Angew. Chem., Int. Ed.* **2017**, *56* (47), 15118−15122.

(36) Furukawa, H.; Gándara, F.; Zhang, Y.-B.; Jiang, J.; Queen, W. L.; Hudson, M. R.; Yaghi, O. M. Water Adsorption in Porous Metal-Organic Frameworks and Related Materials. *J. Am. Chem. Soc.* **2014**, *136* (11), 4369−4381.

(37) Klet, R. C.; Liu, Y.; Wang, T. C.; Hupp, J. T.; Farha, O. K. Evaluation of Brønsted Acidity and Proton Topology in Zr- and Hf-Based Metal-Organic Frameworks Using Potentiometric Acid-Base Titration. *J. Mater. Chem. A* **2016**, *4* (4), 1479−1485.

(38) Yan, X.; Wang, K.; Xu, X.; Wang, S.; Ning, Q.; Xiao, W.; Zhang, N.; Chen, Z.; Chen, C. Brønsted Basicity in Metal − Organic Framework-808 and Its Application in Base-Free Catalysis. *Inorg. Chem.* **2018**, 8033.

(39) Decoste, J. B.; Peterson, G. W.; Jasuja, H.; Glover, T. G.; Huang, Y. G.; Walton, K. S. Stability and Degradation Mechanisms of Metal-Organic Frameworks Containing the $Zr_6O_4(OH)_4$ Secondary Building Unit. *J. Mater. Chem. A* **2013**, *1* (18), 5642−5650.

(40) Maier, L.; Van Wazer, J. R. Principles of Phosphorus Chemistry. *J. Am. Chem. Soc.* **1962**, *84* (16), 3054−3058.

(41) Dietrich, C.; Weber, D. A.; Culver, S.; Senyshyn, A.; Sedlmaier, S. J.; Indris, S.; Janek, J.; Zeier, W. G. Synthesis, Structural Characterization, and Lithium Ion Conductivity of the Lithium Thiophosphate $Li_2P_2S_6$. *Inorg. Chem.* **2017**, *56* (11), 6681−6687.

(42) Toh, R. J.; Sofer, Z.; Pumera, M. Catalytic Properties of Group 4 Transition Metal Dichalcogenides (MX2; M = Ti, Zr, Hf; X = S, Se, Te). *J. Mater. Chem. A* **2016**, *4* (47), 18322−18334.

(43) Ichimura, K.; Sano, M. Electrical Conductivity of Layered Transition-Metal Phosphorus Trisulfide Crystals. *Synth. Met.* **1991**, *45* (2), 203−211.

(44) Dietrich, C.; Koerver, R.; Gaultois, M. W.; Kieslich, G.; Cibin, G.; Janek, J. J.; Zeier, W. G. Spectroscopic Characterization of Lithium Thiophosphates by XPS and XAS-a Model to Help Monitor Interfacial Reactions in All-Solid-State Batteries. *Phys. Chem. Chem. Phys.* **2018**, *20* (30), 20088−20095.

(45) Vechiato-Filho, A. J.; Matos, A. O.; Landers, R.; Goiato, M. C.; Rangel, E. C.; De Souza, G. M.; Barão, V. A. R.; dos Santos, D. M. Surface Analysis and Shear Bond Strength of Zirconia on Resin Cements after Non-Thermal Plasma Treatment and/or Primer Application for Metallic Alloys. *Mater. Sci. Eng., C* **2017**, *72*, 284−292.

(46) Valenzano, L.; Civalleri, B.; Chavan, S.; Bordiga, S.; Nilsen, M. H.; Jakobsen, S.; Lillerud, K. P.; Lamberti, C. Disclosing the Complex Structure of UiO-66 Metal Organic Framework: A Synergic Combination of Experiment and Theory. *Chem. Mater.* **2011**, *23*, 1700−1718.

(47) Kandiah, M.; Nilsen, M. H.; Usseglio, S.; Jakobsen, S.; Olsbye, U.; Tilset, M.; Larabi, C.; Quadrelli, E. A.; Bonino, F.; Lillerud, K. P. Synthesis and Stability of Tagged UiO-66 Zr-MOFs. *Chem. Mater.* **2010**, *22* (24), 6632−6640.

(48) Klipstein, P. C.; Pereira, C. M.; Friend, R. H. Transport and Raman Studies of the Group IV Layered Compounds and Their Lithium Intercalates: Li_xTiS_2, Li_xTiSe_2, Li_xZrS_2, Li_xZrSe_2, Li_xHfS_2 and Li_xHfSe_2. *Philos. Mag. B* **1987**, *56* (5), 531−559.

(49) Zhang, M.; Zhu, Y.; Wang, X.; Feng, Q.; Qiao, S.; Wen, W.; Chen, Y.; Cui, M.; Zhang, J.; Cai, C.; Xie, L. Controlled Synthesis of ZrS 2 Monolayer and Few Layers on Hexagonal Boron Nitride. *J. Am. Chem. Soc.* **2015**, *137* (22), 7051−7054.

(50) Dietrich, C.; Weber, D. A.; Sedlmaier, S. J.; Indris, S.; Culver, S. P.; Walter, D.; Janek, J.; Zeier, W. G. Lithium Ion Conductivity in Li_2S-P_2S_5 Glasses - Building Units and Local Structure Evolution during the Crystallization of Superionic Conductors Li_3PS_4, $Li_7P_3S_{11}$ and $Li_4P_2S_7$. *J. Mater. Chem. A* **2017**, *5* (34), 18111−18119.

(51) Baumann, A. E.; Burns, D. A.; Díaz, J. C.; Thoi, V. S. Lithiated Defect Sites in Zr Metal-Organic Framework for Enhanced Sulfur

Utilization in Li-S Batteries. *ACS Appl. Mater. Interfaces* **2019**, *11* (2), 2159−2167.

(52) Li, Z.; Zhang, J.; Lou, X. W. D. Hollow Carbon Nanofibers Filled with MnO_2 Nanosheets as Efficient Sulfur Hosts for Lithium-Sulfur Batteries. *Angew. Chem., Int. Ed.* **2015**, *54* (44), 12886−12890.

(53) Liu, X.; Huang, J. Q.; Zhang, Q.; Mai, L. Nanostructured Metal Oxides and Sulfides for Lithium-Sulfur Batteries. *Adv. Mater.* **2017**, *29*, 1601759.

(54) Park, H.; Siegel, D. J. Tuning the Adsorption of Polysulfides in Lithium-Sulfur Batteries with Metal-Organic Frameworks. *Chem. Mater.* **2017**, *29* (11), 4932−4939.

(55) Wan, C.; Wu, W.; Wu, C.; Xu, J.; Guan, L. A Layered Porous ZrO_2/RGO Composite as Sulfur Host for Lithium-Sulfur Batteries. *RSC Adv.* **2015**, *5* (7), 5102−5106.

(56) Sun, F.; Wang, J.; Long, D.; Qiao, W.; Ling, L.; Lv, C.; Cai, R. A High-Rate Lithium-Sulfur Battery Assisted by Nitrogen-Enriched Mesoporous Carbons Decorated with Ultrafine La_2O_3 nanoparticles. *J. Mater. Chem. A* **2013**, *1* (42), 13283−13289.

(57) Tao, X.; Wang, J.; Ying, Z.; Cai, Q.; Zheng, G.; Gan, Y.; Huang, H.; Xia, Y.; Liang, C.; Zhang, W.; Cui, Y. Strong Sulfur Binding with Conducting Magnéli-Phase $TinO2n-1$ Nanomaterials for Improving Lithium-Sulfur Batteries. *Nano Lett.* **2014**, *14* (9), 5288−5294.

(58) Prymak, I.; Prymak, O.; Wang, J.; Kalevaru, V. N.; Martin, A.; Bentrup, U.; Wohlrab, S. Phosphate Functionalization of CeO_2-ZrO_2 Solid Solutions for the Catalytic Formation of Dimethyl Carbonate from Methanol and Carbon Dioxide. *ChemCatChem* **2018**, *10* (2), 391−394.

(59) Bensitel, M.; Moraver, V.; Lamotte, J.; Saur, O.; Lavalley, J.-C. Infrared Study of Alcohols Adsorption on Zirconium Oxide: Reactivity of Alkoxy Species towards CO_2. *Spectrochim. Acta Part A Mol. Spectrosc.* **1987**, *43* (12), 1487−1491.

(60) Golubenko, D. V.; Yurova, P. A.; Karavanova, Y. A.; Stenina, I. A. Surface Modification of Zirconia with Acid Groups. *Inorg. Mater.* **2017**, *53* (10), 1053−1057.

(61) Zheng, S.; Zhu, D.; Xu, Z.; Wan, H.; Zong, E.; Tang, Y. Zirconia Functionalized SBA-15 as Effective Adsorbent for Phosphate Removal. *Microporous Mesoporous Mater.* **2012**, *155*, 192−200.

(62) Zheng, Y.; Zheng, S.; Xue, H.; Pang, H. Metal-Organic Frameworks for Lithium-Sulfur Batteries. *J. Mater. Chem. A* **2019**, *7* (8), 3469−3491.